

# Flight dynamics model identification of a meso-scale twin-cyclocopter in hover

Carl Runco<sup>1</sup>  and Moble Benedict<sup>1</sup>International Journal of Micro Air Vehicles  
Volume 15: 1–16  
© The Author(s) 2023  
Article reuse guidelines:  
sagepub.com/journals-permissions  
DOI: 10.1177/17568293231206943  
journals.sagepub.com/home/mav

## Abstract

In this paper the flight dynamics of a 33-gram twin-cyclocopter is analyzed via deriving a Linear Time Invariant (LTI) dynamics model from flight test data. The twin-cyclocopter is a novel micro air vehicle that uses two co-rotating cycloidal rotors to generate thrust and a coaxial nose rotor to counteract the reaction torque and provide additional thrust. During flight tests, perturbation maneuvers were performed about the hovering state to excite different modes and a 3D motion capture system collected attitude and position data. The data was used to extract a bare airframe LTI model linearized about the hovering state using time-domain system identification techniques. The model demonstrated that the roll and yaw modes are gyroscopically coupled with stable high-frequency and low-frequency modes. Comparing the two different yaw control methods: thrust vectoring of the cycloidal rotors and differential torque of the coaxial nose rotor, the former was more effective.

## Keywords

Cyclocopter, cyclorotor, micro air vehicles, system identification, advanced vertical lift

Date received 21 November 2022; accepted: 15 June 2023

## Introduction

It is no secret that small, capable, flying vehicles are growing more popular and more essential to many industries. This is largely because of the rapid developments in electronics and software that greatly improved the performance of these systems thereby transforming them from hobby toys to commercial and even military equipment. This ever-growing field is dominated by one particular type of Micro Air Vehicle (MAV): the multi-copter. Whether it is a quad-, hex-, octo-, or deca-copter the trend is to unwaveringly add or reduce the number of small conventional rotors as needs dictate with seemingly no upper limit (Figure 1).

All this in an effort to produce ever smaller flying craft that can be portable and functional in a world that is constantly in motion. Reduced size enhances portability and expands the profile of potential missions. Lugging around suitcases of equipment is less than desirable for everyone, the average drone enthusiast and military operator alike. Given the choice between a smaller and larger MAV that both serve the same function, more often than not the smaller one will be selected. Furthermore, a reduced footprint could broaden the range of applications for MAVs in both civilian and military sectors. A smaller, lightweight vehicle can be flown indoors where a larger UAV might not be able to maneuver and it can do so with more relative

safety to the people in its vicinity. There is also the opportunity for enhanced clandestine operation when avoiding detection is paramount.

Regardless of the configuration, as traditional MAVs are scaled down they have to contend with the reduced aerodynamic performance of rotors and wings, which limits their flight envelope. The primary aerodynamic limitation of conventional rotors/propellers used in MAVs is their reduced efficiencies at low Reynolds numbers (10,000–50,000), in particular, low values of maximum figure of merit (around 0.65).<sup>1,2</sup> The reduced aerodynamic performance is caused by large profile drag associated with thick boundary layer formations on the blades, large induced losses, and higher rotational and turbulent losses in the downstream wake of the rotating blades.<sup>3,4</sup> MAVs are

<sup>1</sup>Texas A&M University, College Station, Texas, USA

### Corresponding authors:

Carl Runco, Texas A&amp;M University Advanced Vertical Flight Laboratory, College Station, Texas, USA.

Email: carl.runco@gmail.com

Moble Benedict, Texas A&amp;M University Advanced Vertical Flight Laboratory, College Station, Texas, USA.

Email: benedict@tamu.edu





Figure 1. Multicopter drone design utilizing eight rotors.

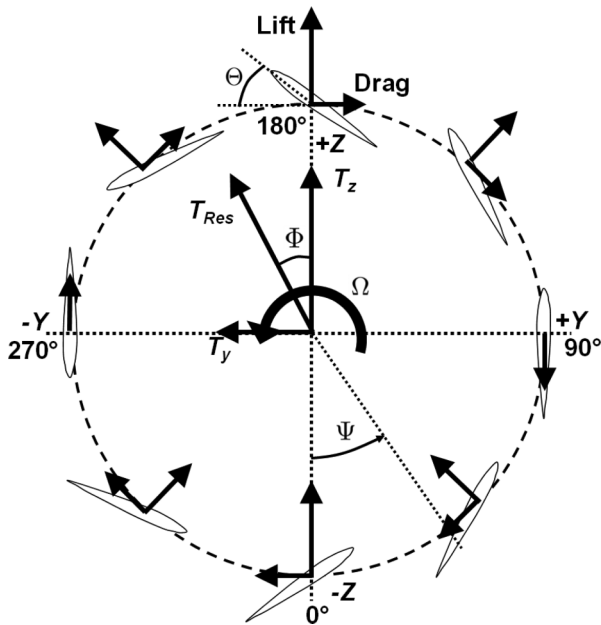


Figure 2. Blade kinematics and forces on a cyclorotor.

also highly susceptible to disturbances such as wind gusts because of their lower inertia. As an aerial vehicle is scaled down its rotational inertia are reduced by  $L^5$ ,  $L$  being some characteristic length, but the aerodynamic forces are only reduced by  $L^2$ , making the aircraft much more sensitive to gusts. Consequently, greater control authority and faster actuator response times are necessary to stabilize these smaller vehicles.

It is for these reasons that significant motivation exists to investigate further into unconventional thrust generation and control techniques, including various out-of-the-box propulsion concepts such as flapping wings and cycloidal rotors (or cyclorotors). The focus of this paper is application of the cyclorotor, which is a non-traditional concept that consists of several blades that rotate about a horizontal axis with the blade span parallel to the axis of rotation.

Figure 2 illustrates how the pitch angle of each blade is varied periodically as it moves around the azimuth of the cyclorotor such that the blade is at a positive geometric angle of attack both at the top and bottom halves of its

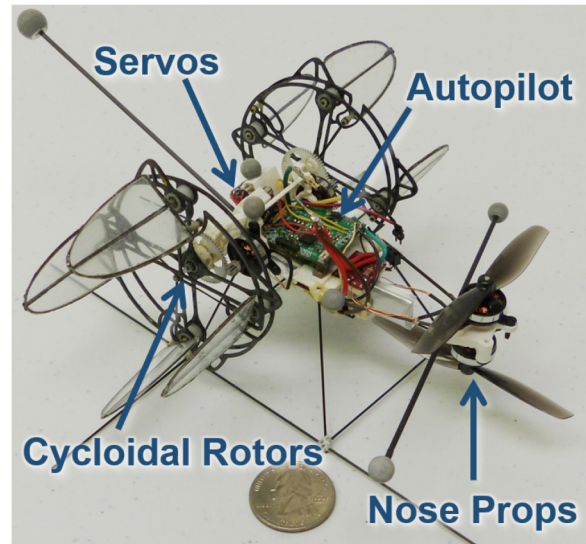


Figure 3. Micro Twin-Cyclocopter with coaxial nose rotors.

circular trajectory. The magnitude and direction of the net thrust vector of the cyclorotor can be changed by varying the amplitude and phase of the cyclic blade pitch. Since the thrust vector of a cyclorotor can be instantaneously set to any direction perpendicular to the rotational axis, the concept may also have better maneuverability compared to conventional rotor based MAVs, which makes it ideal for highly constrained indoor operations and gusty outdoor environments.

Cyclorotor-based platforms have been built at sizes ranging from 30 grams to hundreds of kilograms for mobility in both aerial and aquatic environments. Research into the use of cyclorotors for MAVs has demonstrated their superior performance in comparison to conventional rotors. For example, extensive experimental studies<sup>5</sup> have shown that a cyclorotor may be more aerodynamically efficient than a conventional rotor of the same scale. This is in part due to the fact that all the spanwise elements of the blade operate at the same aerodynamic conditions, allowing each of the blade elements to be set at its optimum condition. Previous aerodynamic studies performed by the author cyclorotors<sup>6-12</sup> have included detailed performance measurements and flow-field analysis using Particle Image Velocimetry (PIV). These were done in an effort to understand the force production and optimize the aerodynamic efficiency of MAV-scale cyclorotors. Additionally, an aeroelastic model to predict the hover performance of a cyclorotor has been developed and validated.<sup>13</sup> The cyclorotor used for the research presented in this paper is the smallest of the referenced cyclorotors (as well as the smallest one built to date) and has a unique design (Figure 3).

In order to scale down the cyclorotor concept, a rigorous parametric study was conducted to optimize performance at the desired operating range. PIV-based flow field measurements were also performed to understand the complex

3-dimensional flow that is unique to the scaled down design.<sup>12</sup> These optimized cyclorotors have been incorporated into a twin-cyclocopter platform that has demonstrated stable, hovering flight.<sup>14</sup> The current 33-gram vehicle is one of a family of cyclocopter MAVs developed by the authors that utilizes this specialized cyclorotor (Figure 4).

While system identification has been done previously on a larger 550-gram cyclocopter to obtain a Linearized Time Invariant (LTI) dynamics model,<sup>15</sup> this new vehicle is significantly different due to its size and design and, therefore, warrants a thorough investigation. Because of the significantly lower mass and rotational inertia, this 33-gram cyclocopter exhibits faster dynamics, a greater degree of gyroscopic coupling, and unexpected responses to benign commands. As such, a dynamical model could reveal much about this type of aircraft. The LTI model can be used to quantify the flight performance of the micro-cyclocopter in order to understand how the inherent dynamics change when the vehicle is scaled down and also to compare the cyclocopter MAV to conventional rotary-wing MAVs of similar scales. Additionally, such a model can be used to develop improved model-based control strategies, conduct simulations, and extract maneuverability and disturbance rejection metrics.<sup>15</sup> This paper details the process used to extract a bare airframe model through systematic flight

testing followed by a discussion of the results. A bare airframe model captures the response of the vehicle to natural physics and control actuator effectiveness agnostic of any control system implementation or stability augmentation. A brief description of the design and development of the vehicle is provided prior to the discussion of the system identification experiment.

## Vehicle design and development

On this small-scale device several design choices were made to take advantage of its diminutive nature. Inspired by tiny fliers found in nature, these cyclorotors were crafted with cantilevered blades that somewhat resemble insect wings. Qualities that emulate insects include the low aspect ratio elliptical planform shape and flat-plate airfoil that has higher performance at these low Reynolds numbers ( $\sim 11,000$ ) when compared to traditional airfoils.<sup>16</sup> These blades are constructed via a mold-layup process using carbon fiber pre-preg that produces consistent results. The main spar is a unidirectional carbon fiber rod while the planform frame is made with thin strips of unidirectional pre-preg. This places the chordwise CG (center of gravity) very close to the mid-chord of the blade, coincidental with the pitching axis, which eliminates blade torsion

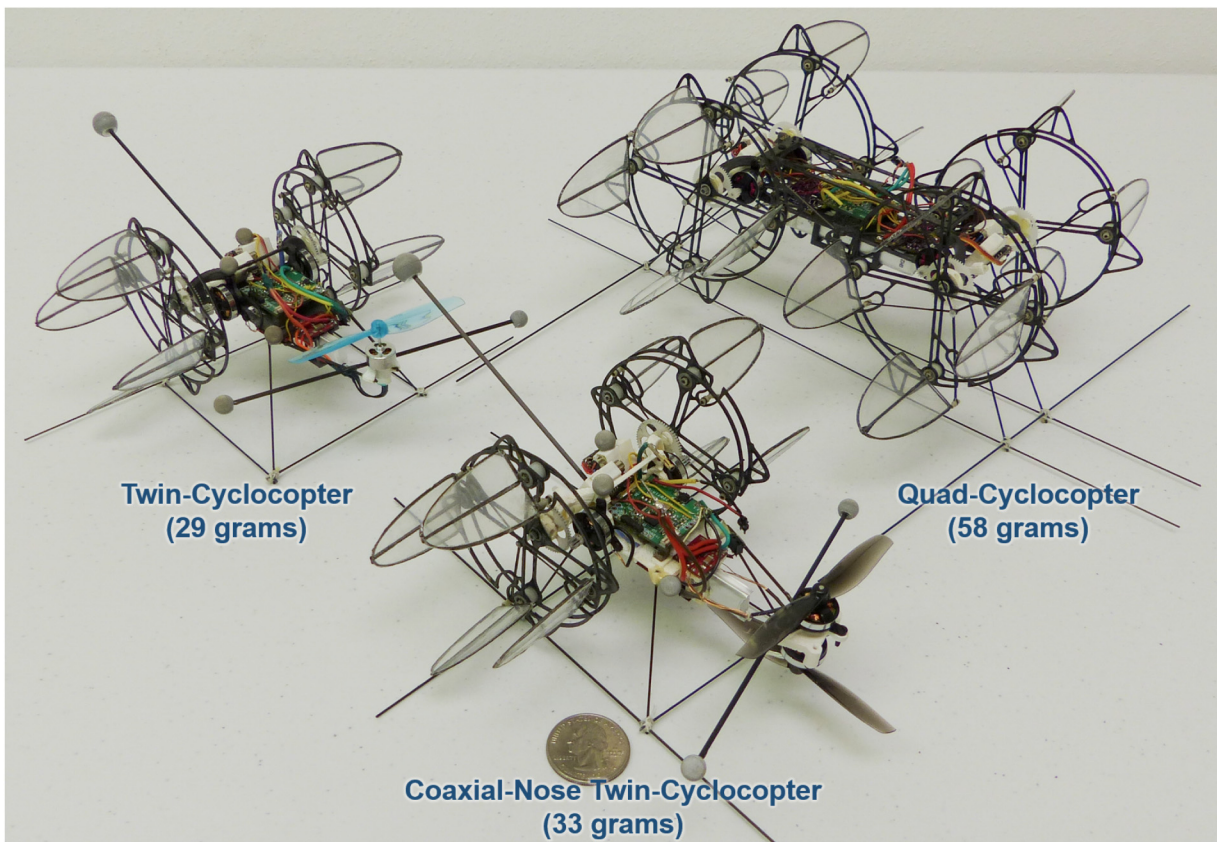


**Figure 4.** Hover-capable cyclocopters developed by the authors.

and control loads from inertial forces. A 3 micron thick mylar sheet is then affixed to the blade with contact cement. This process produced ultra-lightweight blades (0.1 gram each) with excellent bending and torsional stiffness, both of which are critical because any flexibility in the blades will drastically reduce performance.<sup>13</sup>

The blades are secured to the endplate structure via a Delrin<sup>®</sup> spacer that has two micro-bearings and a PEEK bushing (Figure 5). Linkages made via a similar mold-layup process are connected to the pitch horn with additional PEEK (polyether ether ketone) bushings and are part of a 4-bar linkage mechanism housed between the two 1/32" carbon fiber end plates so that it is secure in the event of a hard landing, unlike the distally mounted linkages seen in larger cyclocopter designs. A blade pitch amplitude of  $\pm 45^\circ$  is implemented. The body is rapid-prototyped, producing a light-weight, stiff core to which all of the electronics are

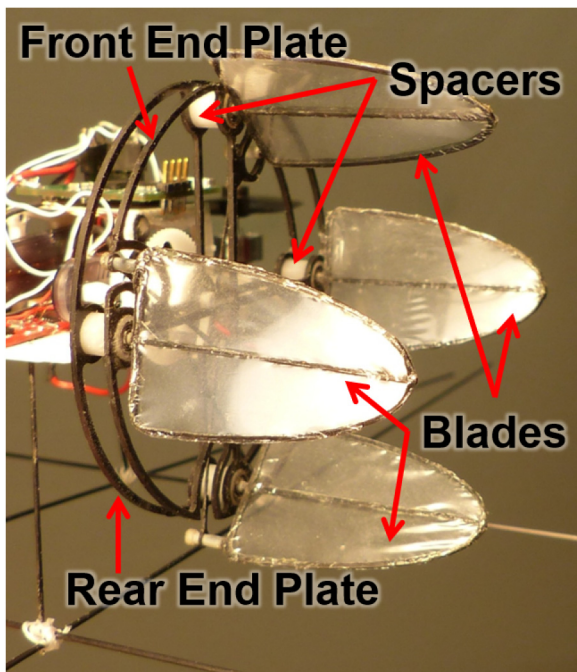


Figure 5. Micro-cyclocopter with components labelled.

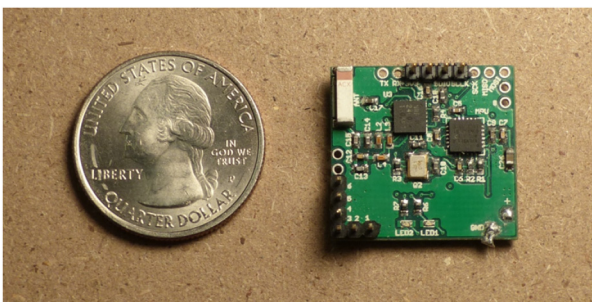


Figure 6. Custom built 1.3-gram kinematic autopilot with U.S. quarter for size comparison.

mounted. All of the electronic components are off-the-shelf hardware except for the flight controller (Figure 6), which is a custom autopilot developed at the University of Maryland.<sup>17</sup> More details on the flight controller are provided later in the paper. The flight controller was mounted as close to the CG as possible so that the accelerometer and gyro measurements could be used without any corrections.

### Coaxial nose rotor

Previous studies<sup>18,19</sup> have characterized the performance and flowfield of the small cyclocopters used on these vehicles as well as validated the hover performance of the 29-gram twin-cyclocopter configuration shown in Figure 4. All of the previous twin-cyclocopter vehicles had a single nose rotor. Reference 20 also outlines efforts to capture the flight dynamics of that single nose rotor twin-cyclocopter. That study showed a high-degree of coupling partially because of the gyroscopic moments. The unbalanced yaw torque and angular momentum of the single nose rotor meant that any rolling or pitching motion produced an off-axis moment that made the dynamics highly coupled and non-linear, which resulted in poor handling qualities for the vehicle. In response to this, a second counter-rotating rotor was added to balance the torque and angular momentum generated about the vertical axis of the vehicle. This ameliorated the aforementioned gyroscopic couplings, fully isolating the pitching motion from the roll and yaw directions. Moreover, now it was not needed to counteract the unbalanced torque from the single nose rotor by canting the thrust vectors of the cyclocopters, which helped reduce the impact of variations in cyclocopter rpm on yaw. Another practical benefit resulting from the reduction in coupling is the fact that during flight testing a stable hover trim can be achieved significantly faster because cyclocopter thrust vectors can be trimmed independently of the nose propellers and pitch trim. To date, this is the only twin-cyclocopter built with coaxial nose rotors, prompting this study into its flight dynamics. A weight breakdown of this 33-gram vehicle is shown in Table 1.

### Flight tests

The first step to prepare the vehicle for system identification is to trim it around the state of interest, which in this case is

Table 1. Component Weight Breakdown.

Component	Weight (g)	Total (%)
Motors + Transmission	7.5	23
Cyclocopters (Combined)	6.2	19
Structure + Wires	4.7	14
Li-Po Batteries	4.9	15
Electronics	4.1	12
Nose Rotors + Motors	5.6	17
Total	33	100

hover. The present twin-cyclorotor configuration has 6 controls: four motor speeds and two cyclorotor thrust directions controlled by the servo actuators, making this an over-actuated system. There are many potential advantages to this (e.g., maneuverability and disturbance rejection) that have been investigated in Refs. 15,20.

### Attitude control

In order to understand how the vehicle is controlled and trimmed a short summary of the attitude control strategy is presented. The magnitude and direction of forces and moments are controlled through altering motor speeds and thrust-vectoring servos in specific combinations to control roll, pitch, and yaw. The body axes are defined as shown

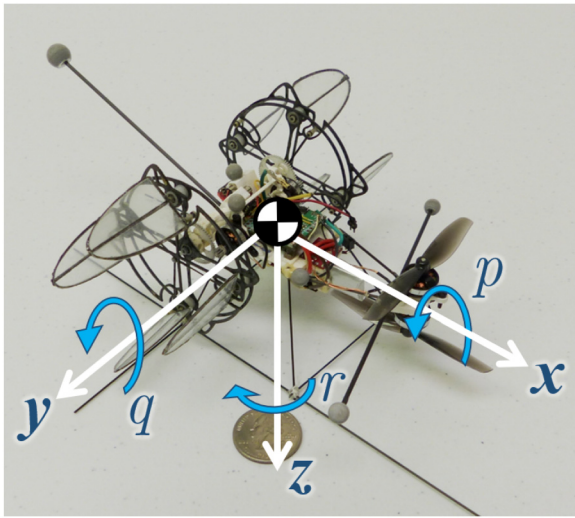


**Figure 7.** Micro-cyclocopter with body axis frame shown and corresponding positive body angular rates.

in Figure 7 where the coaxial rotor is considered the front of the aircraft.

**Roll:** Roll is controlled by differentially changing the rpm of the cyclorotors, which changes the relative magnitude of the thrust, generating a rolling moment. (Figure 8).

**Pitch:** A pitch moment is created by increasing the rpm of both nose rotors simultaneously (Figure 9), which increases their thrust and creates a pitching moment about the vehicle CG.

**Yaw:** Because of the over-actuation there are two methods that can be used to generate a yawing moment. The first is by using the servos, which can independently vary the phasing of the blade cyclic pitch schedule for each of the two cyclorotors and thereby vector their thrust (Figure 10). The second method involves making opposing adjustments to the upper and lower nose rotor rotation speeds (Figure 11).

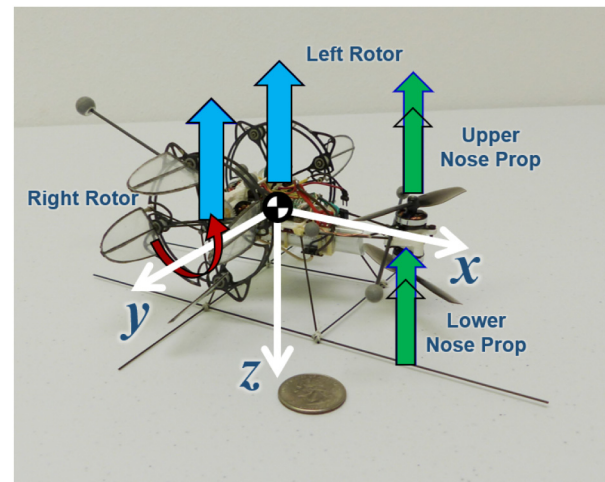


**Figure 9.** A positive pitch moment generated by increasing nose rotor thrust.

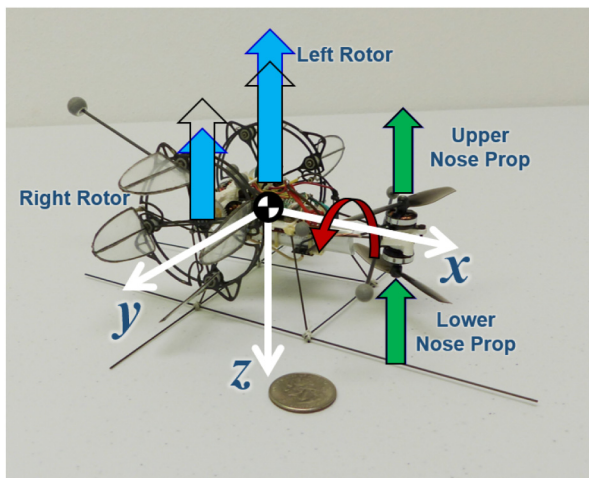


**Figure 8.** A positive roll moment generated by changing thrust of the cyclorotors.

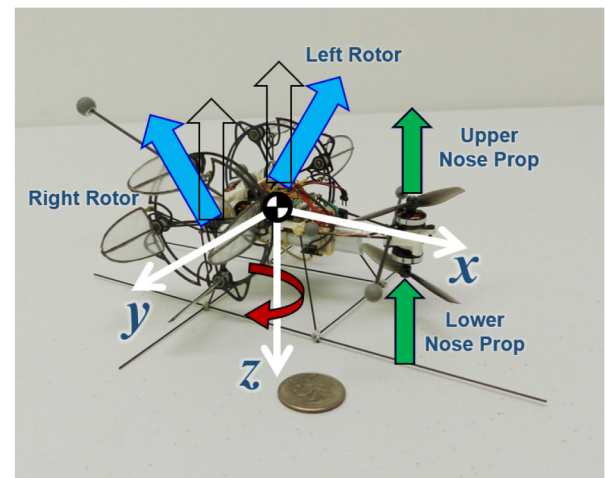


**Figure 10.** A positive yaw moment generated by vectoring cyclorotor thrust.

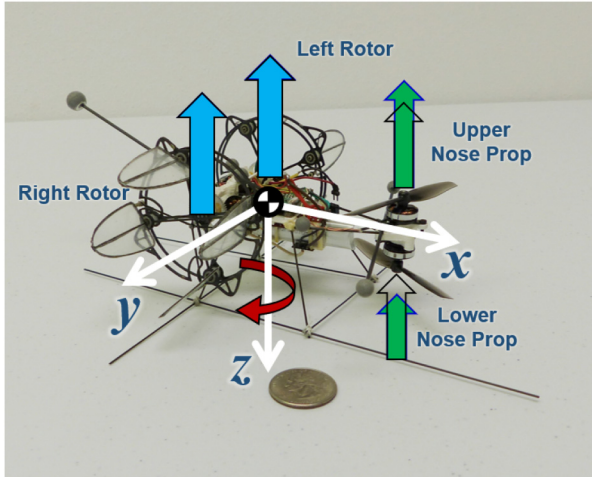


**Figure 11.** A positive yaw moment generated by offsetting nose rotor thrust to generate torque.

The upper nose rotor spins counterclockwise so an increase in its rpm increases the clockwise reaction torque on the body. The opposite holds true for the lower rotor.

### Trimming

Unfortunately, due to over-actuation, the vehicle has multiple trim states that result in level flight; however, only one eliminates constant drift as well as controller-induced couplings. Finding the proper trim state can be a challenging task. Specifically, in the case of the micro-cyclocopter, it is not easy to assess small variations in the direction of the net thrust vector. This is the primary reason why the present configuration uses a counter-rotating coaxial rotor in the front instead of a single rotor like the 29-gram vehicle in Figure 4. By eliminating the nose rotor yaw torque there is no need to differentially vector the cyclocopter thrust to counteract it, which means that trimming for hover demands perfectly vertical thrust vectors ( $\Phi = 0$ ). To facilitate setting this, a single-axis yaw stand (shown with vehicle mounted in Figure 12) is first used to balance the torque of the nose rotors without rotating the cyclocopters. Fortunately, the rpm offset required for the nose rotors remained nearly constant across all throttle settings resulting in a balanced yaw torque across the entire throttle range. Then, on the same stand, the cyclocopters are each spun-up independently (with nose rotors not rotating) and the blade pitch phasing servo positions were individually adjusted at hover throttle until the vehicle experienced no yawing motion. This implied that the two cyclocopter thrust vectors were vertical. From the trim setting attained in this manner only minor subsequent corrections off of the stand were required to reach the desired trim in flight, assessed by performing short hops until vertical take-off was achieved.

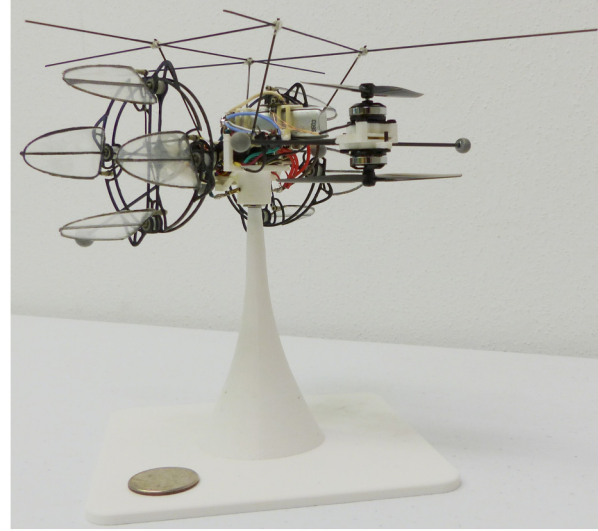


**Figure 12.** Micro-cyclocopter mounted upside-down on single axis yaw stand.

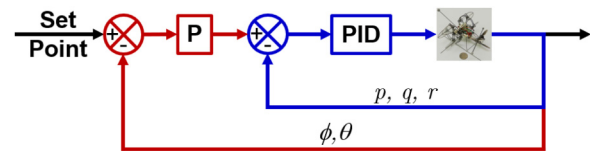


**Figure 13.** Feedback loop architecture for normal test flight operations.

### Feedback

Once the vehicle was successfully trimmed for hovering flight, feedback gains were introduced in order to provide an additional level of stability augmentation necessary beyond a human pilot's capability in order to automatically stabilize the attitude of the vehicle. These strategies were implemented on a custom-designed flight control board that used an STM32F4 micro-processor with gyros and accelerometers to sense body axis rotational rates and accelerations. These data were used in a cascaded loop structure as shown in Figure 13. Roll and pitch were stabilized by experimentally tuned PPID control loops (PID: Proportional-Integral-Derivative) that stabilized the vehicle about a desired angle. For the outer P loop, commands from the transmitter were converted to a desired body angle by a linear equation. Error between the commanded angle and the measured angle was then multiplied by the outer P gain to produce a desired body angular rate, which became the input for the inner PID loop. Because heading angle was not measured, no outer P loop was implemented for yaw and the associated transmitter commands were converted to a desired body angular rate as the input for a PID loop.

Pilot inputs and trims are sent through a base station that concurrently collects vehicle telemetry from the flight,

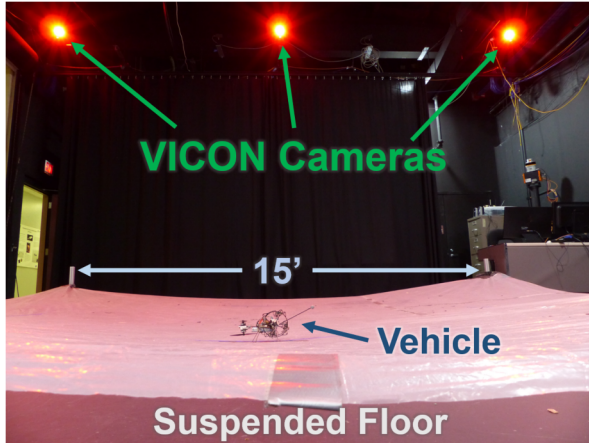


**Figure 14.** Flight space with suspended floor and Vicon cameras.

while also performing several other functions. Hover being the desired state for this experiment, effort was focused on reducing constant drift and yaw. All flight tests were conducted in a specially arranged space measuring  $15 \times 15$  ft with a plastic suspended floor that protected the vehicle in the event of a crash or hard landing (Figure 14). A sample flight video can be found at Ref. 21.

### Flight dynamics identification

Having achieved stable, hovering flight, preparations had to be made for the collection of data that would allow the extraction of a bare airframe LTI model. Linear system identification involves perturbing the vehicle from a trim state (hover in this case), recording the control input and system response, and deriving linearized equations of motion to model the system response with the vehicle states. Reference 22 explains the process of linearizing the non-linear aircraft equations of motion about a desired equilibrium point using Taylor Series expansion. The result is the familiar linear state space equation:

$$\dot{\mathbf{x}} = \mathbf{A}\mathbf{x} + \mathbf{B}\mathbf{u} \quad (1)$$

where  $\mathbf{A}$  is the matrix representing the body dynamics and  $\mathbf{B}$  characterizes the response to control inputs. The vector  $\mathbf{x}$  is the state vector and  $\mathbf{u}$  is the control vector defined as:

$$\mathbf{x} = [u \ v \ w \ p \ q \ r \ \phi \ \theta \ \psi] \quad (2)$$

$$\mathbf{u} = [\delta_{lat} \ \delta_{lon} \ \delta_{dir_{TV}} \ \delta_{dir_{\Delta Q}} \ \delta_{thr} \ \delta_{phase}] \quad (3)$$

The entries in  $\mathbf{x}$  are the collected translational velocities and angular rates in the body frame and the Euler angles. Integrating the on-board accelerometers to get body axis velocities would generate unacceptable error; therefore, a Vicon motion capture system consisting of six cameras around the flight space (Figure 14) was used to track the vehicle states using reflective beacons attached to the vehicle (the small grey spheres shown in Figure 3).

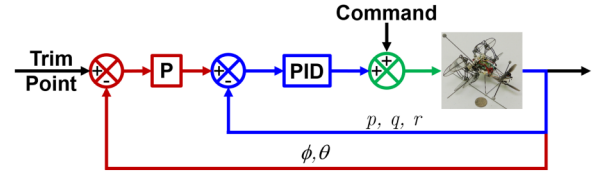


**Figure 15.** Feedback loop architecture for system identification experiments and data collection.

Inertial position  $[X_i, Y_i, Z_i]$  and Euler parameter data  $[\beta_0, \beta_1, \beta_2, \beta_3]$  of the vehicle were captured during flight and sent to the base station to be synced with the data from the flight controller. A small adjustment of about 30 ms is needed to account for latency between the Vicon data and onboard sensors. With this information, the time history of the inertial position can be converted to velocities and accelerations in the body frame.

The values in  $\mathbf{u}$  are control inputs scaled to be in the range of  $[-1, 1]$  which should allow the results of this experiment to be compared to other models regardless of actuator type. Collectively, entries in  $\mathbf{u}$  and  $\mathbf{x}$  are known as regressors. Finding the non-zero indices in the  $\mathbf{A}$  and  $\mathbf{B}$  matrices associated with each regressor is done using the SIDPAC<sup>®</sup> software suite developed by Dr. Morelli for MATLAB<sup>®</sup>.<sup>23</sup> This method has been successfully used to quantify the behavior of everything from statically stable aircraft to unstable aircraft like the F-16 and even non-traditional systems like flapping wing vehicles and other cyclocopters.<sup>15,24,25,22</sup> Time domain methods were used because space constraints and the system's unstable nature limited the ability to perform frequency sweeps and other maneuvers with enough spectral content for frequency domain analysis.<sup>22</sup>

### Data collection

A modified loop structure is used to control the cyclocopter during data collection that allows for the derivation of a model that is independent of controller implementation (Figure 15). This loop more closely comports with the assumptions of linear analysis, particularly the assumption that the vehicle is always driven back to a trim point. As such, the control inputs in  $\mathbf{u}$  are the total combined input comprising of controller and pilot commands. This means that the pure actuator input is being correlated to the system output. However, closed-loop feedback has poor a signal-to-noise ratio and can corrupt the system dynamics and, as a result, the controller gains needed to be lowered as much as possible. Through experimentation it was found that this small cyclocopter was passively stable in roll and yaw and, therefore, it could be flown with no gains for those degrees of freedom, which is the ideal situation for this experimental methodology. Pitch, being unstable, required feedback to stabilize but feedback gains

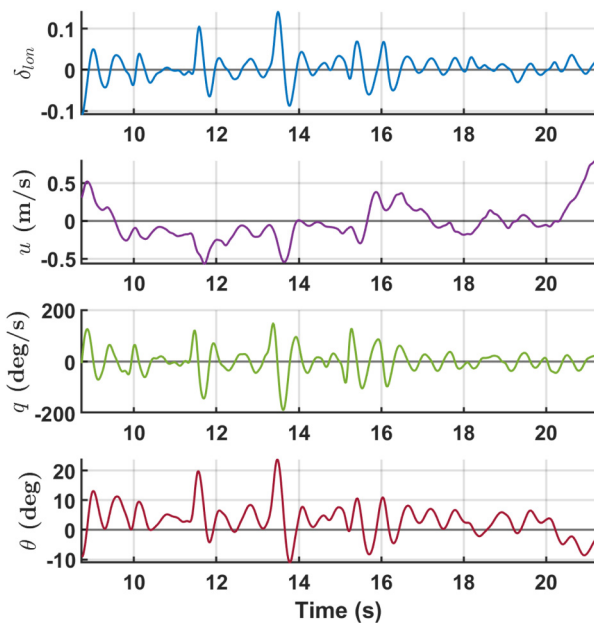
were reduced from typical flight gains as much as possible and no integral or derivative gains were used.

The perturbations to excite the various modes of the system were provided by the pilot rather than generated by a computer because it was imperative to prevent the craft from going unstable and human inputs tend to contain a broader spectral character.<sup>26</sup> Various input methods were compared: doublets of various periods, frequency sweeps, and impulses. No benefit was observed in data quality or model accuracy by using more complicated inputs so simple impulses were the preferred method of excitation. A sample of flight test data can be seen in Figures 16 to 19. The data was filtered using a 4<sup>th</sup> order Butterworth filter with a 6 Hz cutoff frequency. It is easy to identify the location of the control inputs (or perturbations) and the associated vehicle response, not only in the corresponding mode, but in the other modes as well (e.g., a yaw response can be observed when a roll input is given). These data are all from the same flight test shown for the same period of time.

Within these, a periodic motion in roll and yaw can be seen that is not associated with any control input (Figure 17). This motion is part of the open-loop dynamics and develops naturally from a stationary hover. It was noted in flight testing that an increase in throttle damped this mode out and eliminated it during vertical ascent. Conversely, a descent seemed to induce or exacerbate this motion.

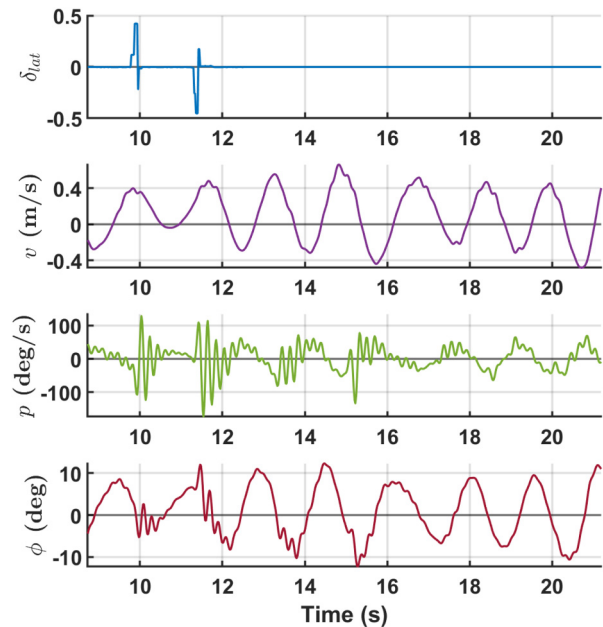
### Linear model

Over 50 sets of similar data were collected in this manner and analyzed using the SIDPAC<sup>®</sup> code. This code linearly



**Figure 16.** Representative flight test data for longitudinal perturbation experiment.

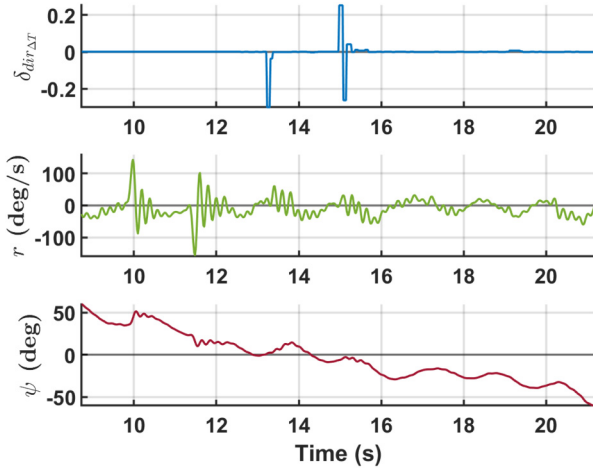
relates the vector of measured regressors with their derivatives using a least squares fit. To help the researcher select meaningful and well-correlated parameters in the matrix, SIDPAC<sup>®</sup> displays two primary metrics. One is F-ratio and the other is the coefficient of determination ( $R^2$ ). The F-ratio is a measure of how well the variance in the data is captured by a regressor and a value above 20 gives a 95% confidence level. If a selected regressor generated a value less than this, it was excluded from the model. Through a process known as stepwise regression, parameters are chosen in each equation for the given regressor. The coefficient of determination quantifies the error between data and model of selected regressors and is expressed as a percentage between 0 and 100 — a higher value is better. In addition to these factors judgment on the part of the experimentalist is required to combine these metrics with knowledge of the system to appropriately determine which parameters to include. There is no hard cut-off for  $R^2$  values and a high F-ratio does not always mean that the parameter should be included. Drift or other experimental idiosyncrasies can induce a correlation where one is not actually present. Furthermore, certain elements of the matrix can be excluded based on vehicle symmetry. An example that illustrates both of these points is potential correlation between the  $u$  velocity and lateral acceleration,  $\dot{v}$ , that did appear in several data sets. A disturbance could generate a response that artificially would appear correlated; however, because of the cyclocopter's symmetry about the XZ-plane there should be no physical reason as to why the platform would preferentially develop a sideslip in one direction over the other. Alternatively, in



**Figure 17.** Representative flight test data for lateral perturbation experiment.

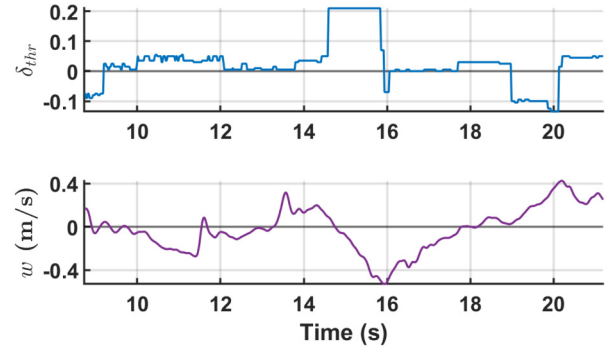
**Table 2.** Parameter Values for Coaxial-Nose Twin-Cyclocopter.

Parameter	Value	% STD
Longitudinal Mode		
$X_u$	-0.60	25
$X_{phase}$	3.05	5
$M_u$	4.25	38
$M_w$	4.71	44
$M_q$	-1.75	43
$M_{lon}$	-248.84	11
$M_{dir\Delta Q}$	-41.46	33
$M_{thr}$	21.16	43
Lateral Mode		
$Y_v$	-0.50	32
$L_v$	-19.55	36
$L_p$	-2.73	29
$L_r$	18.60	24
$L_{lat}$	76.77	45
Directional Mode		
$N_v$	-11.83	32
$N_p$	-11.14	19
$N_r$	-2.35	26
$N_{lat}$	-33.45	45
$N_{dirTV}$	50.88	59
$N_{dir\Delta Q}$	25.51	40
Heave Mode		
$Z_u$	-0.48	37
$Z_q$	-0.30	52
$Z_{lon}$	5.47	40
$Z_{thr}$	-2.81	37

**Figure 18.** Representative flight test data for directional perturbation experiment.

several cases, a parameter did not appear well correlated for a singular set of data, but in the aggregate emerged often enough that it was included in the averaged results.

It was this fusion of a academic prudence and quantitative investigation that produced the model structure shown below. The associated values for these parameters are

**Figure 19.** Representative flight test data for heave perturbation experiment.

shown in Table 2. The discerning reader might wonder how the two values for yaw control,  $\delta_{dirTV}$  (differential cyclorotor thrust vectoring) and  $\delta_{dir\Delta Q}$  (differential nose rotor torque), were separated in the controls matrix given that they both excite the same vehicle mode. Only one was required at a time to control yaw and therefore one half of the experiments were run with one type of yaw control and the other half with the other type. The  $A$  matrices extracted from both were very similar, as was expected, and the only differences in the  $B$  matrices were the corresponding parameters. Because of the linear nature of this analysis they can be combined into one  $B$  matrix.

$$\begin{pmatrix} \dot{u} \\ \dot{v} \\ \dot{w} \\ \dot{p} \\ \dot{q} \\ \dot{r} \\ \dot{\phi} \\ \dot{\theta} \\ \dot{\psi} \end{pmatrix} = \begin{bmatrix} X_u & 0 & 0 & 0 & 0 & 0 & 0 & -g & 0 \\ 0 & Y_v & 0 & 0 & 0 & 0 & g & 0 & 0 \\ Z_u & 0 & 0 & 0 & Z_q & 0 & 0 & 0 & 0 \\ 0 & L_v & 0 & L_p & 0 & L_r & 0 & 0 & 0 \\ M_u & 0 & M_w & 0 & M_q & 0 & 0 & 0 & 0 \\ 0 & N_v & 0 & N_p & 0 & N_r & 0 & 0 & 0 \\ 0 & 0 & 0 & 1 & 0 & 0 & 0 & 0 & 0 \\ 0 & 0 & 0 & 0 & 1 & 0 & 0 & 0 & 0 \\ 0 & 0 & 0 & 0 & 0 & 1 & 0 & 0 & 0 \end{bmatrix} \begin{pmatrix} u \\ v \\ w \\ p \\ q \\ r \\ \phi \\ \theta \\ \psi \end{pmatrix} + \begin{bmatrix} 0 & 0 & 0 & 0 & 0 & X_{phase} \\ 0 & 0 & 0 & 0 & 0 & 0 \\ 0 & Z_{lon} & 0 & 0 & Z_{thr} & 0 \\ L_{lat} & 0 & 0 & 0 & 0 & 0 \\ 0 & M_{lon} & 0 & M_{dir\Delta Q} & M_{thr} & 0 \\ N_{lat} & 0 & N_{dirTV} & N_{dir\Delta Q} & 0 & 0 \\ 0 & 0 & 0 & 0 & 0 & 0 \\ 0 & 0 & 0 & 0 & 0 & 0 \\ 0 & 0 & 0 & 0 & 0 & 0 \end{bmatrix} \begin{pmatrix} \delta_{lat} \\ \delta_{lon} \\ \delta_{dirTV} \\ \delta_{dir\Delta Q} \\ \delta_{thr} \\ \delta_{phase} \end{pmatrix}$$

Having derived a linear model it is important to see its predictive capabilities. To that end, Figures 20 and 21

show a sample of data with the model output overlaid. In general, the model tracks the test data well, particularly for the larger disturbances. Although there is a slight amplitude mismatch in the higher frequency content, overall the model does a good job of predicting vehicle dynamics.

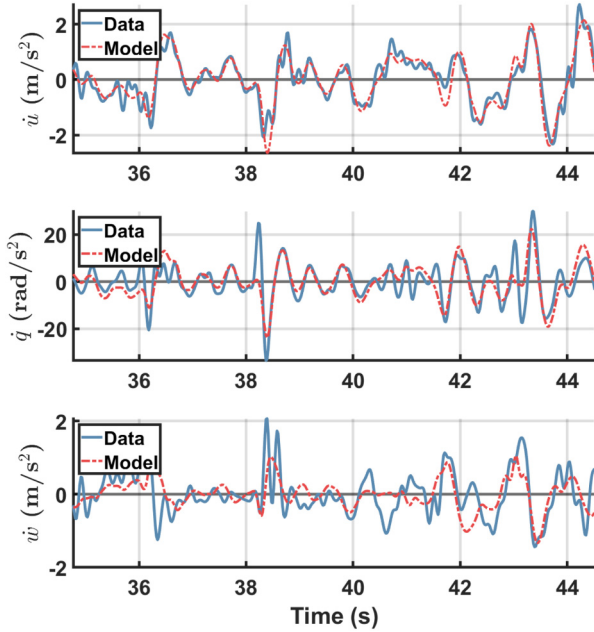


Figure 20. Sample of longitudinal data with model prediction.

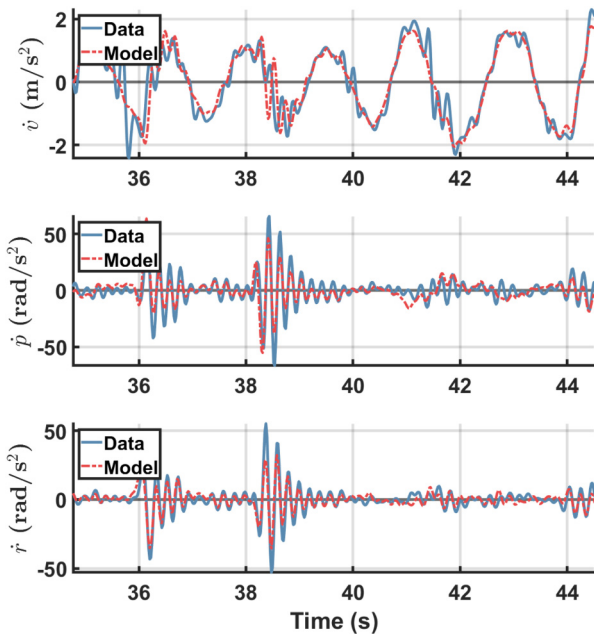


Figure 21. Sample of lateral data with model prediction.

### Discussion

Many insights can be gained from analyzing the derived model. One of the best places to start is the model structure itself. An emergent pattern of the parameters is apparent. The repeated parameters across lateral and directional equations show that they are gyroscopically coupled by the cyclorotors. Longitudinal and heave modes also contain a common set of parameters. The lack of shared terms between these pairs of modes shows that they are decoupled from each other. This is proven in the Eigenvalue analysis of the  $A$  matrix, shown in Table 3.

There are two open-loop stable lateral oscillatory modes (one high frequency and one low), an unstable oscillatory longitudinal mode, a stable longitudinal mode, and a neutrally stable translational mode. Of additional interest is the impact of the feedback gains on flight stability and these modes. Taking the same gains used during data collection and plugging them into the formula,  $A - BK$ , the closed-loop poles can be calculated from the resulting matrix. The open and closed loop poles are plotted in Figure 22 for comparison, from which it can be seen that the feedback gains on pitch manage to shift the longitudinal modes barely into the stable region, thus validating that feedback gains were reduced as much as possible to the edge

Table 3. Eigenvalues for open loop dynamics.

Mode	Eigenvalue	Frequency (Hz)
Lateral: $p$	$-2.18 \pm 13.89i$	2.24
Lateral, Directional: $v, p, r$	$-0.61 \pm 3.58i$	0.58
Longitudinal: $u, q$	$0.74 \pm 3.11i$	0.51
Longitudinal: $u, q, \theta$	$-4.33$	—
Longitudinal, Heave: $u, w$	$0.50$	—

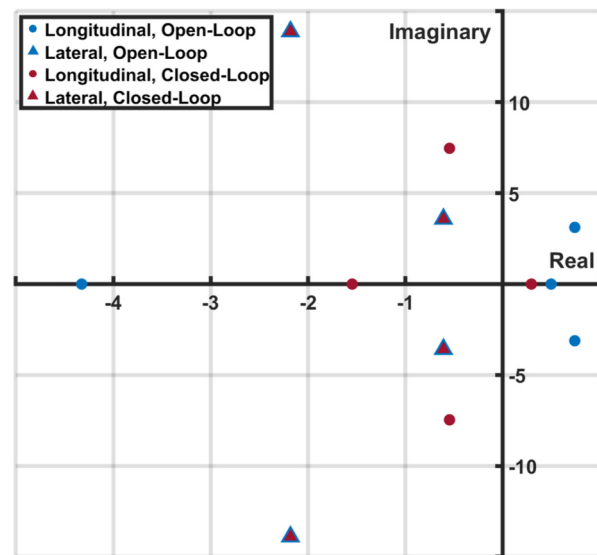
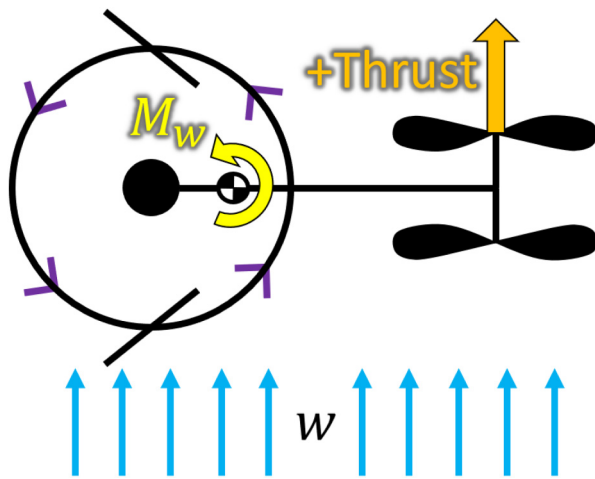


Figure 22. Pole plot showing open-loop poles and the impact of gains on stability.

of stability. Lateral/directional modes remain unchanged because there were no feedback gains in those degrees of freedom. Next, each mode will be discussed individually in more detail.

### Longitudinal mode

The previously mentioned efforts to decouple pitch from other flight modes by balancing the Z-axis torque of the nose rotor are apparent in the isolated nature of this mode. The most characteristic feature about this degree of freedom is its instability. The singular unstable mode for this model is present in this direction, hence the



**Figure 23.** Schematic showing the free flow for a positive  $w$  velocity and resulting moment.

need for feedback control during flight. The  $M_u$  and  $M_w$  terms in the  $A$  matrix provided in Table 2 can be easily explained: the positive  $M_u$  is caused by the resulting nose-up moment from the nose rotors in edge-wise flight; and the  $M_w$  parameter can be explained by a change of inflow resulting from vertical motion. With a positive  $w$  perturbation (vehicle descent leads to velocity increasing from below the nose rotor), the inflow velocity through the nose rotor will decrease (because it will subtract from the hover inflow velocity), resulting in an increase in angle of attack and thus the thrust. The increase in thrust at the nose rotor will result in a nose-up moment (Figure 23).

### Lateral and directional mode

The gyroscopic coupling present in these modes is a characteristic property of cyclocopters because of their large angular momentum. The off-diagonal terms,  $L_r$  and  $N_p$ , being nearly an order of magnitude higher than the damping terms along the diagonal shows how much the vehicle motion is driven by this gyroscopic effect.

More interestingly, one unique characteristic learned through these efforts is revealed by the  $L_p$  term. Previous twin-cyclocopters that have been built and flown were open-loop unstable in roll.<sup>15</sup> The vehicle in this study is open-loop stable in roll and it is the negative  $L_p$  term that stabilizes the roll degree of freedom. The hypothesized reason for this disparity lies in design differences between the cyclocopters. Figure 24 shows several cyclocopters developed at the University of Maryland by the author.<sup>27,28</sup> The dissimilarity between these cyclocopters and the one developed in this study arose during the process of scaling it down. Most prominently, the rectangular planform blade

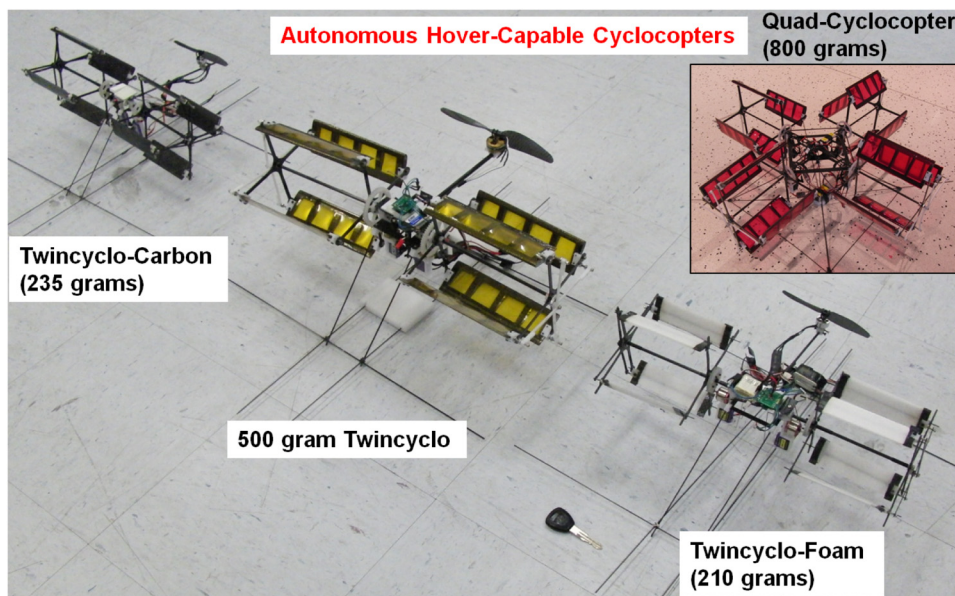


**Figure 24.** Previous hover capable cyclocopters developed by the author.

supported at both ends was changed to a cantilevered design, which means there are no endplates to support the blade tips.

As a result, the cyclorotors are completely open at one end, altering the flowfield around the cyclorotors by allowing axial flow into the current cantilevered design whereas it is blocked by the spinning end plate structure in all the previous doubly supported designs. Evidence of this can be seen in PIV studies that were previously conducted by the authors.<sup>9,12</sup> A small amount of axial inflow is induced by the current cantilevered design (Figure 25). Along with the typical 2D inflow, this axially ingested flow makes a 90° turn and aligns with the inflow of the cyclorotor adding to the total mass flow through the cyclorotor. However, when the vehicle encounters a sideslip velocity ( $v$ ) the spanwise inflow could increase, which will further augment mass flow and hence the thrust of the cyclorotor. Such a phenomenon would lead to a rolling moment opposite the sideslip direction, producing a stabilizing mode. As the vehicle rolls it develops a lateral velocity  $v$  due to a change in  $\phi$ . The sideslip velocity increases the mass flow rate for the cyclorotor that is pointing towards the sideslip direction thereby increasing its thrust. Conversely, for the leeward cyclorotor the effect is opposite and it might experience reduced thrust. This could result in the low

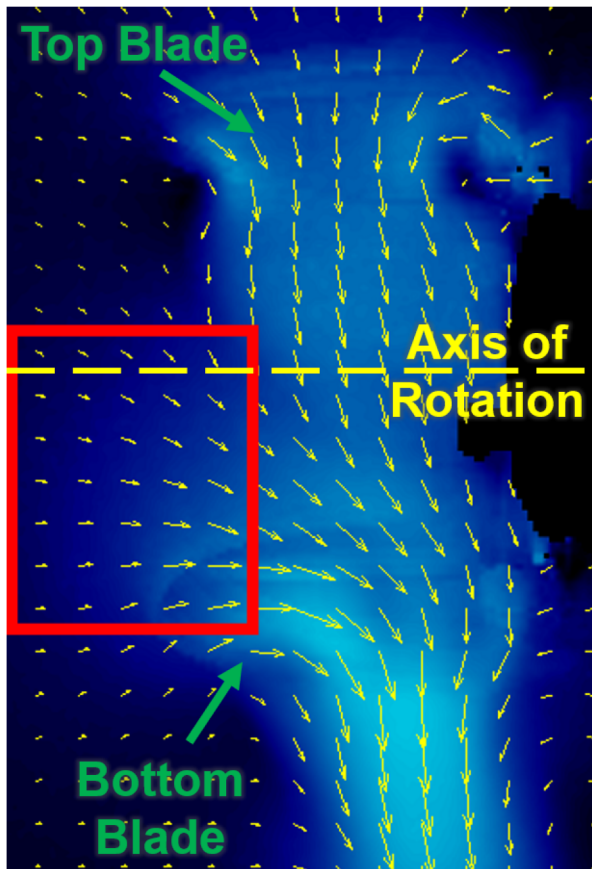


**Figure 25.** PIV snapshot with region of induced axial flow shown inside the red box.

frequency pendulum mode in roll that can be seen in Figure 17 with a time period of about 2 seconds. This is the only study that has demonstrated passive roll stability in MAV-scale cyclocopters.

Along with this low frequency mode there is an accompanying, naturally occurring high frequency mode in the roll degree of freedom likely caused by inflow changes during roll. The presence of these modes complicated the flight testing operations, particularly the tuning of feedback gains. If the gains were too low there was not enough control to damp out the low frequency mode. But too much feedback led to the excitation of the inherent high frequency mode. For normal flight operations, roll and yaw gains must be tuned carefully to balance between these limiting phenomena.

### Heave mode

A couple of intriguing things can be seen in the heave degree of freedom. First, is the lack of a damping term ( $Z_w$ ) along the diagonal which means that vertical damping is so small that it did not appear in the linear analysis. The second is the presence of a  $Z_u$  term which captures a phenomenon called virtual camber caused by a flat airfoil experiencing curvilinear flow. Figure 26 shows how this changes the effective camber (or virtual chordline) of the rotating blades at different azimuthal locations, represented by the red lines. What this means is that a forward velocity,  $u$ , has a different impact on the top blade than it does on the bottom one. The outcome is a greatly increased lift on the lower blade and slightly decreased lift on the upper one, producing a net positive lift. If the direction of flow is reversed (i.e., the cyclocopter moves backwards) the top blade would experience a slight increase in lift, but the bottom blade would suffer a large loss in lift leading to a net reduction in thrust. Because of this, the “nose” rotor should be considered the front of the vehicle

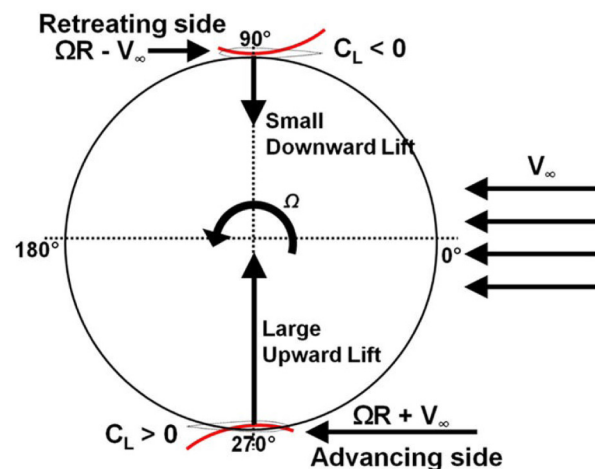


**Figure 26.** Net positive thrust due to a cyclorotor with bottom blade advancing into the freestream caused by virtual camber.

for efficient forward flight. More details on the virtual camber effect can be found in Ref. 29.

Naturally, an increased lift in the rear of the vehicle due to virtual camber should cause a negative (nose down) pitching moment. However, there is actually a positive pitching moment ( $M_u$ ) in response to forward flight which must mean that some other physics beyond edgewise flight of the nose rotors, such as wake interaction, is having a greater impact. When in forward flight,  $+u$  could be pushing the downwash of the upper nose rotor away from the lower one (skewed downwash), reducing the wake interaction on the lower rotor generating more thrust and hence, a positive pitching moment (Figure 27). In the opposite case of  $-u$  (flying reverse), the wake created by the body of the vehicle and the cyclorotors could be interacting with the nose rotors and reducing their thrust, and causing a negative pitching moment.

### Control methodology

While the primary focus of this research was to analyze the bare airframe dynamics, there are several important insights that can be gained from the extracted control parameters as well. Taking a look at the  $B$  matrix, the most obvious thing to note is the relative magnitude of  $M_{lon}$  with respect to all other entries. This parameter is substantially larger indicating more sensitivity in pitch to control inputs. A second peculiarity is the presence of  $M_{thr}$  which represents the varying response rates of the cyclorotors relative to the nose rotors and the resulting change in torque from changing cyclorotor rotational speed. In normal flight this was taken advantage of by combining changes in cyclorotor torque with nose rotor thrust to command pitch. This combination method can also be tuned for balanced net thrust (e.g., reducing cyclorotor thrust in response to an increased nose rotor thrust) effectively canceling out the  $Z_{lon}$  term. Similarly, when using differential nose rotor torque to control yaw, pitch commands ( $\delta_{lon}$ ) can be coupled to differential torque yaw commands ( $\delta_{dir\Delta Q}$ ) to eliminate the natural tendency of the coaxial-nose rotors to produce a pitching moment in response to differential RPM

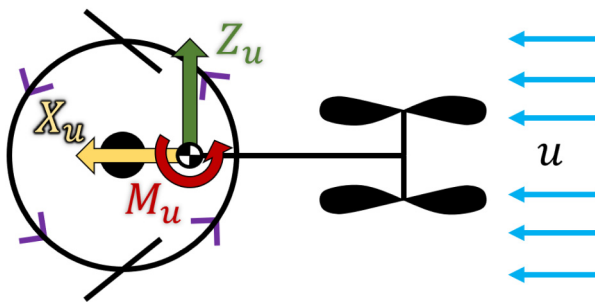


**Figure 27.** Total effective forces and moments created by a forward velocity.

adjustments ( $M_{dir\Delta Q}$ ). Flight control software implemented for normal flight operations leveraged these observations to improve performance. To do so, empirically generated lift vs rpm and rpm vs control input curves were used for the nose rotors and cyclorotors to calculate any change in net thrust due to a pitch or yaw command. For pitch, cyclorotor thrust was used to offset the change in nose rotor thrust so that total thrust remained the same ( $Z_{lon} = 0$ ) while simultaneously augmenting the pitching moment with cyclorotor torque. For a yaw command using differential nose rotor torque, the change in rpm demanded of the nose rotors was adjusted such that the total lift remained approximately constant ensuring little to no accompanying pitch ( $M_{dir\Delta Q} = 0$ ). These relations are not linear, which would reduce correlation during the linear least squares analysis and prevent the controls derivatives from being identified accurately. To improve the extracted model, the described relations were removed during experimental data collection.

One parameter that might seem counter intuitive is  $N_{lat}$ . Considering efforts were made to ensure the cyclorotor thrust vectors were vertical, there should be no yaw torque produced by a roll command. But roll is controlled by differentially adjusting the rpm of the cyclorotors and cyclorotor thrust vectors inherently change direction with rpm as a byproduct of their rotational nature and flow interaction within the cyclorotor itself. Therefore a change in rpm is nearly equivalent to using the servos to tilt the lift vectors, which is also why  $N_{lat}$  is approximately the same magnitude as  $N_{dirTV}$ .

**Thrust vectoring parameters.** Unique to the cyclorotor is the ability to vector the thrust by changing the phase of cyclic blade pitch — governed on the coaxial-nose twin-cyclocopter by the position of its two servos — thus permitting two forms of control. The first is produced by obverse motion of the servos to generate a yawing moment,  $\delta_{dirTV}$ . The second is from tandem operation generating a longitudinal force that results in translation without pitching,  $\delta_{phase}$ . It is poignant to note in the control matrix that both only impact one degree of freedom, whereas all of the other control parameters produce responses in more than one.

**Yaw Control:** Because this is the first twin-cyclocopter to incorporate a coaxial-nose it was not obvious what, if any, benefit might be gained by having redundant control strategies for yaw when previous twin-cyclocopters had been stabilized and flown with only thrust vectoring yaw control. Quantifying the behavior of the separate yaw control methods characterized some of the difference between them, providing insight into the properties of the cyclocopter. Most apparent is the enhanced control effectiveness of thrust vectoring versus differential torque as a means of yaw stabilization and control ( $N_{dirTV} > N_{dir\Delta Q}$ ), but the linear model does not capture their full nature. In

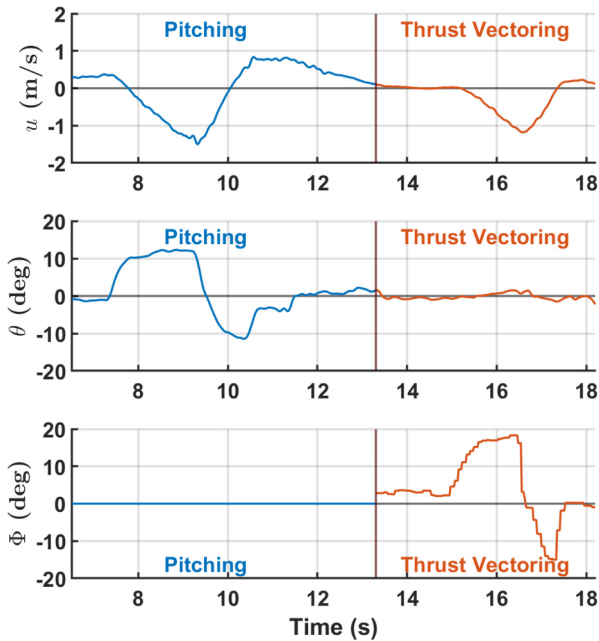


**Figure 28.** Test data showing longitudinal motion achieved via pitching and thrust vectoring in a single flight.

practice, the disparate frequency responses between the motors and servos provided a complimentary effect rather than a redundant one. The faster response time of the motors compared to the servos made differential torque control suited to the low amplitude, high frequency regime, while thrust vectoring control achieved via servos was more suited to the high amplitude, low frequency regime. Separate PID gains were used for each, allowing them to be tuned more precisely for the associated response. Increased control authority in the high frequency range accounts for some of the dramatic improvement of flight quality in the coaxial-nose twin-cyclocopter compared to the single nose rotor configuration, especially considering that the reduced scale of the micro-cyclocopter makes high frequency disturbances more prevalent.

**Longitudinal Translation:** Figure 28 presents a comparison of forwards and backwards motion achieved by pitching and thrust vectoring. In the first several seconds, pitch attitude ( $\theta$ ) is adjusted to produce longitudinal velocity ( $u$ ), typical of traditional multirotor MAVs. From approximately the 13 second mark onward the vehicle is commanded to maintain a constant pitch attitude while thrust phase angle of the cyclorotors ( $\Phi$ ) is augmented to create longitudinal motion. In the former case, all thrust vectors (cyclorotors and nose rotors) are angled into the direction of motion, but in the latter the nose rotor thrust remains vertical and only the cyclorotor thrust generates longitudinal acceleration. As explained earlier, the velocity created by longitudinal flight increased lift production ( $Z_u$ ) and resulted in a pitch-up moment ( $M_u$ ) meaning that nose rotor rpm could be reduced. The combination of induced lift and

reduced power consumption potentially make forward flight an energy efficient flight mode for the cyclocopter. High speed forward flight might further benefit from thrust vectoring translation due to the reduced drag profile presented by the vehicle at a level pitch attitude.

## Conclusions

In this paper the flight dynamics of a 33-gram micro twin-cyclocopter in a hovering state were investigated via extracting a bare airframe Linear Time-Invariant (LTI) dynamic model from flight test data using time-domain system identification techniques. The current twin-cyclocopter, owing to its small size, cantilevered blade design, and counter-rotating coaxial-nose rotors, is a unique design configuration with significantly improved handling qualities, all of which make it distinct from other cyclocopters that have been built in the past. Previously flown cyclocopters developed by the authors were several times heavier, used doubly-supported rectangular blades, and utilized only a single nose rotor each. The aggregate effects of the reduced inertia, unique cyclorotor aerodynamics, and absence of nose rotor reaction moment allowed the micro twin-cyclocopter to demonstrate passive roll stability. The first and only cyclocopter to do so to date. The LTI model encapsulates many of these qualities in a simplified set of equations representing a complex dynamical system. A mode and frequency analysis was done on the system of equations that showed two stable modes and one unstable oscillatory mode. The key lessons learned from this study are enumerated below.

1. A torque and angular momentum balanced nose rotor system minimizes coupling, simplifies the trimming process, and significantly improves the handling qualities of the twin-cyclocopter.
2. The current micro twin-cyclocopter was observed to be inherently (open-loop) stable in roll with two oscillatory modes.
3. A strong gyroscopic coupling was experienced between roll and yaw due to the large unbalanced angular momentum of the cyclorotors.
4. Smart control techniques were used to take advantage of the coupled nature of this vehicle to improve performance.

## Funding

This research was partially supported by the U.S. Army's Micro Autonomous Systems and Technology–Collaborative Technology Alliance (MAST-CTA) with Chris Kroninger (Army Research Laboratory–Vertical Technology Directorate) as Technical Monitor.

The work was also partially supported by Army/Navy/NASA's Vertical Lift Research Center of Excellence (VLRCE) led by the University of Maryland with Dr. Alex Moodie and Dr. Mahendra Bhagawat as Technical Monitors.

## Declaration of conflicting interests

The authors declare that there are no potential conflicts of interest with respect to the research, authorship, and/or publication of this article.

## Funding

The author(s) received no financial support for the research, authorship and/or publication of this article.

## ORCID iD

Carl Runco  <https://orcid.org/0000-0002-1759-4496>

## References

- Pines DJ and Bohorquez F. Challenges facing future micro-air-vehicle development. *J Aircr* 2006; 43: 290–305.
- Chopra I. Hovering micro air vehicles: Challenges and opportunities. In *Proceedings of American Helicopter Society Specialists' Conference*. Seoul, Korea: International Forum on Rotorcraft Multidisciplinary Technology.
- Leishman JG. *Principles of helicopter aerodynamics*. New York, NY: Cambridge University Press, 2006.
- Ramasamy M, Johnson B and Leishman JG. Understanding the aerodynamic efficiency of a hovering micro-rotor. *J Am Helicopter Soc* 2008; 53: 412.
- Benedict M, Jarugumilli T and Chopra I. Experimental optimization of MAV-scale cycloidal rotor performance. *J Am Helicopter Soc* 2011; 56: 22005–2200511.
- Sirohi J, Parsons E and Chopra I. Hover performance of a cycloidal rotor for a micro air vehicle. *J Am Helicopter Soc* 2007; 52: 263–279.
- Benedict M, Jarugumilli T and Chopra I. Design and development of a hover-capable cyclocopter mav. In *Proceedings of the 65th Annual National Forum of the American Helicopter Society*. Grapevine, TX. 27–29.
- Benedict M, Ramasamy M, Chopra I et al. Experiments on the optimization of the mav-scale cycloidal rotor characteristics towards improving their aerodynamic performance. In *Proceedings of the International Specialists' Meeting on Unmanned Rotorcraft*. Scottsdale, Arizona. 20–22.
- Benedict M, Ramasamy M, Chopra I et al. Performance of a cycloidal rotor concept for micro air vehicle applications. *J Am Helicopter Soc* 2010; 55: 22002–2200214.
- Benedict M, Jarugumilli T and Chopra I. Experimental performance optimization of a mav-scale cycloidal rotor. In *Proceedings of the AHS Specialists' Meeting on Aeromechanics*. San Francisco, CA, pp. 20–22.
- Walther C, Coleman D, Benedict M et al. Experimental and computational studies to understand unsteady aerodynamics of cycloidal rotors in hover at ultra-low reynolds numbers. In *AHS International 73rd Annual Forum & Technology Display*. Fort Worth, Texas, USA: AHS International.
- Runco C, Himmelberg B and Benedict M. Performance and flowfield measurements of a meso-scale cycloidal rotor in hover. In *AHS International 73rd Annual Forum & Technology Display*. Fort Worth, Texas, USA: AHS International.
- Benedict M, Mattaboni M, Chopra I et al. Aeroelastic analysis of a micro-air-vehicle-scale cycloidal rotor in hover. *AIAA J* 2011; 49: 2430–2443.
- Runco C, Coleman D and Benedict M. Development of the world's smallest cyclocopter. In *Proceedings of the AHS International's 72nd Annual Forum Technology Display*. West Palm Beach, Florida.
- Hrishikeshavan V, Benedict M and Chopra I. Identification of flight dynamics of a cyclocopter micro air vehicle in hover. *J Aircr* 2015; 52: 116–129.
- Winslow J, Otsuka H, Govindarajan B et al. Basic understanding of airfoil characteristics at low reynolds numbers (104–105). *J Aircr* 2017; 55: 1050–1061.
- Hrishikeshavan V and Chopra I. Refined lightweight inertial navigation system for micro air vehicle applications. *Int J Micro Air Vehicles* 2017; 9: 124–135. DOI: 10.1177/1756829316682534.
- Runco CC, Himmelberg B and Benedict M. Experimental studies on a mesoscale cycloidal rotor in hover. *J Aircr* 2018; 1–10. DOI: 10.2514/1.c034736.
- Runco CC, Coleman D and Benedict M. Design and development of a 30 g cyclocopter. *J Am Helicopter Soc* 2019; 64: 1–10.
- Runco C and Benedict M. System identification of a meso-scale twin-cyclocopter in hover. In *Proceedings of the 74th Annual National Forum of the American Helicopter Society*. Phoenix, Arizona.
- Runco C and Benedict M. World's smallest cyclocopter (texas a&m university). <https://www.youtube.com/watch?v=WTUCCkTcIW0>, 2016. URL <https://www.youtube.com/watch?v=WTUCCkTcIW0>.
- Morelli E. Practical aspects of the equation-error method for aircraft parameter estimation. In *AIAA Atmospheric Flight Mechanics Conference and Exhibit*. American Institute of Aeronautics and Astronautics. DOI:10.2514/6.2006-6144.
- Morelli E. System identification programs for AirCraft (SIDPAC). In *AIAA Atmospheric Flight Mechanics Conference and Exhibit*. American Institute of Aeronautics and Astronautics. DOI:10.2514/6.2002-4704.
- Coleman D and Benedict M. Flight dynamics identification, maneuverability, and gust tolerance of a robotic hummingbird in hover. In *Proceedings of the AHS International's 75th Annual Forum Technology Display*. Philadelphia, PA.
- Humbert JS and Faruque I. Analysis of insect-inspired wing-stroke kinematic perturbations for longitudinal control. *J Guid Control Dyn* 2011; 34: 618–623.
- Tischler MB and Remple RK. *Aircraft and Rotorcraft System Identification: Engineering Methods with Flight Test Examples*. 2nd ed. AIAA Education Series, New York: AIAA, 2006. ISBN 1600868207. DOI:10.2514/4.861352. [https://www.ebook.de/de/product/21252622/mark\\_b\\_tischler\\_aircraft\\_and\\_rotorcraft\\_system\\_identification\\_engineering\\_methods\\_with\\_flight\\_test\\_examples.html](https://www.ebook.de/de/product/21252622/mark_b_tischler_aircraft_and_rotorcraft_system_identification_engineering_methods_with_flight_test_examples.html).
- Benedict M, Gupta R and Chopra I. Design, development, and open-loop flight-testing of a twin-rotor cyclocopter micro air vehicle. *J Am Helicopter Soc* 2013; 58: 1–10.
- Benedict M, Shrestha E, Hrishikeshavan V et al. Development of a micro twin-rotor cyclocopter capable of autonomous hover. *J Aircr* 2014; 51: 672–676.
- Benedict M, Jarugumilli T, Lakshminarayan V et al. Effect of flow curvature on forward flight performance of a micro-air-vehicle-scale cycloidal-rotor. *AIAA J* 2014; 52: 1159–1169.

**Nomenclature**

$A$	State matrix	$\mathbf{x}$	State vector
$B$	Control matrix	$Y$	Body-axis lateral force
$C_L$	Coefficient of lift	$Z$	Body-axis vertical force
$K$	Gain matrix	$\beta_0, \beta_1, \beta_2, \beta_3$	Euler parameters (Quaternions)
$L$	Body-axis rolling moment	$\delta_{lat}$	Lateral control input
$L$	Length scale factor; also body-axis rolling moment	$\delta_{lon}$	Longitudinal control input
$M$	Body-axis pitching moment	$\delta_{dirTV}$	Direction control input via thrust vectoring
$N$	Body-axis yawing moment	$\delta_{dir\Delta Q}$	Directional control input via differential nose rotor torque
$p$	Body-axis roll rate	$\delta_{phase}$	Tandem phasing of cyclorotor thrust
$q$	Body-axis pitch rate	$\delta_{thr}$	Throttle input
$R$	Radius of cyclorotor	$\Theta$	Blade pitch angle
$R^2$	Coefficient of determination	$\theta$	Pitch angle
$r$	Body-axis yaw rate	$\Psi$	Cyclorotor azimuthal location
$T$	Thrust	$\psi$	Yaw angle
$\mathbf{u}$	Control vector	$\Phi$	Phase angle of thrust from vertical
$u$	Body-axis longitudinal velocity	$\phi$	Roll angle
$V_\infty$	Freestream velocity	$\Omega$	Cyclorotor rotation speed
$v$	Body-axis lateral velocity	LTI	Linear Time Invariant
$w$	Body-axis vertical velocity	MAV	Micro Air Vehicle
$X$	Body-axis longitudinal force	PEEK	Polyether Ether Keytone
$X_i, Y_i, Z_i$	Inertial position of CG	PID	Proportional-Integral-Derivative
		SIDPAC <sup>®</sup>	System IDentification Programs for AirCraft
		UAV	Uninhabited Aerial Vehicle